

# **Reconstruction of the high resolution phase in a closed loop adaptive optics system**

**R. Ke, R. Wagner, R. Ramlau, R. Chan**

**RICAM-Report 2019-19**

# Reconstruction of the high resolution phase in a closed loop adaptive optics system

Abbreviated: Reconstructing closed loop high resolution phases

Rihuan Ke\*, Roland Wagner†, Ronny Ramlau‡, Raymond Chan§

## Abstract

Adaptive optics (AO) is a commonly used technique to correct the phase distortions caused by the Earth's atmosphere to improve the image quality of the ground-based imaging systems. However, the observed images still suffer from the blur caused by the adaptive optics residual wavefront. In this paper, we propose a model for reconstructing the residual phase in high resolution from a sequence of deformable mirror data. Our model is based on the turbulence statistics and the Taylor frozen flow hypothesis with knowledge of the wind velocities in atmospheric turbulence layers. A tomography problem for the phase distortions from different altitudes is solved in order to get a high quality phase reconstruction. We also consider inexact tomography operators resulting from the uncertainty in the wind velocities. The wind velocities are estimated from the deformable mirror data and, additionally by including them as unknowns in the objective function. To solve the associated joint optimization problem, we use an alternating minimization method which results in a high resolution reconstruction algorithm with adaptive wind velocities. Numerical simulations are carried out to show the effectiveness of our approach.

## 1 Introduction

The modern telescopes allow the acquisition of high resolution images of astronomical objects seen on the night sky. To increase the resolution, ground-based extremely large telescopes (ELTs) with a primary mirror bigger than 30 m in diameter are currently under construction. However, the image quality is still degraded due to the turbulent atmosphere above these telescopes. As a remedy for this degradation, Adaptive Optics (AO) systems were introduced, see, e.g., [10, 7].

An astronomical AO system is a hardware-based device that uses deformable mirrors (DM) to compensate for distortions of the incoming phase due to atmospheric turbulence

---

\*Department of Applied Mathematics and Theoretical Physics, University of Cambridge, Wilberforce Road, Cambridge CB3 0WA, UK.

†Industrial Mathematics Institute, Johannes Kepler University, Altenberger Strasse 69, 4040 Linz, Austria.

‡Industrial Mathematics Institute, Johannes Kepler University, Altenberger Strasse 69, 4040 Linz, Austria and Johann Radon Institute for Computational and Applied Mathematics, Altenberger Strasse 69, 4040 Linz, Austria.

§College of Science, City University of Hong Kong, Kowloon, Hong Kong.

and therefore making the observed images sharper. The DMs are adjusted according to the data from wavefront sensors (WFS) which measure the incoming wavefront from so-called guide stars, which is the phase measured in a specific wavelength. However, due to several physical limitations, the distortions by atmospheric turbulence can never be compensated completely. First, the WFS have a rather coarse resolution as enough light of the guide star has to reach each pixel of the WFS to acquire accurate data. As a consequence, the higher spatial frequencies of the wavefront are not sensed and thus cannot be corrected by the deformable mirror. Second, the correction of the wavefront is also limited by the DM, the shape of which is controlled by a finite number of actuators. Finally, a time gap exists between the acquisition of wavefront data and the update of the DM shape. The atmospheric turbulence is changing rapidly and the increment of the distorted wavefront within the time gap is not taken into account. The uncorrected part of the wavefront, called the residual wavefront, results in a residual blur of the observed image.

Further improvement on the quality of the observed image can be made by image post-processing with data from the AO systems. According to the Fourier optics model (see, e.g., [15, 17]), in an incoherent imaging system, the blurred image is formed by the convolution of the point spread function (PSF) and the true image. The PSF can be determined by the residual wavefront, or the residual phase. Several techniques known as deconvolution methods (see, e.g., [18, 5, 6, 8]) have been developed. Such methods rely on accurate PSF knowledge in order to remove the blur from the observed image. An estimate of the PSF can be computed from the WFS data (see, e.g., [29]) or the reconstructed residual wavefronts [31, 30], which always requires the use of a simulation step for the spatial frequencies of the residual wavefront that are not sensed by the WFS.

The problem of reconstructing a high resolution phase using WFS data has been studied by Chu et al. [6]. In their work, an open loop system is considered and the high resolution gradients of the phase are computed from WFS data at multiple time steps by doing a least square data fitting with Tikhonov regularization. The high resolution phases are then reconstructed using the computed gradients. Their approach uses the knowledge of the wind velocities which are assumed to be known exactly.

The core issue of this paper is to find a high resolution residual phase in a closed loop adaptive optics system which can then be used to obtain a PSF estimate with existing methods. The high resolution residual phase has the capacity of capturing the higher spatial frequencies needed for a more accurate PSF. We make use of the commonly adopted Taylor frozen flow (TFF) assumption [27] to relate a sequence of low resolution AO data to the high resolution phase with the wind velocities. A variational regularization method based on the turbulence statistics and the TFF assumption is developed. The wind velocities might not be available in reality. To preserve the consistency between the TFF and the data, we take the wind velocities as variables of the objective function instead of fixed values. The minimization of the objective function therefore produces estimations of the high resolution phase and the wind velocities simultaneously.

In image processing, the high resolution problem which aims for restoring a high resolution image from a sequence of the low resolution ones has been attracting much interest (see, e.g., [4, 11]). It has been used in a variety of practical applications such as video enhancement, facial image analysis or medical image processing [21].

The remainder of this paper is organized as follows: In Section 2, we describe the problem setting and clarify the notation. In Section 3, a model is proposed based on the turbulence statistics and the Taylor frozen flow hypothesis, by assuming the wind

velocities are known in advance. In order to handle the underlying tomography problem with inexact tomography operators due to the uncertainty in the wind velocities, we also consider adjusting the wind velocities from the DM data using our model. In Section 4, the minimization problem induced by our model is considered. We implement an alternating direction algorithm for computing estimations of the residual phase and the wind velocities. Finally, Section 5 displays the simulated AO system and the numerical results.

## 2 Problem modeling

There exist different configurations of AO systems. Throughout this paper, we focus on Single-Conjugate Adaptive Optics (SCAO) systems. An SCAO system consists of one WFS, one DM and a control unit, which in particular computes the DM shape from data obtained by the WFS. We assume that the SCAO system under consideration is run in closed loop, meaning that WFS is located in the optical path after the DM and thus sees only a residual of the incoming phase. Let us denote the incoming phase at time  $t$  as  $\phi(\mathbf{x}, t)$  where  $\mathbf{x} \in \mathbb{R}^2$  in the pupil plane. Let  $\phi^{\text{DM}}(\mathbf{x}, t)$  be the DM shape and  $\phi^{\text{res}}(\mathbf{x}, t)$  be the residual phase, then it holds that

$$\phi^{\text{res}}(\mathbf{x}, t) = \phi(\mathbf{x}, t) - \phi^{\text{DM}}(\mathbf{x}, t), \quad (1)$$

for  $\mathbf{x}$  inside the telescope pupil. For a reconstruction of  $\phi^{\text{res}}$ , we need the data from the AO system. The remainder of this section is dedicated to the WFS model and the idea of using DM shapes as measurements.

### 2.1 WFS model

In a closed loop AO system, information of the residual phase is collected by the WFS. A variety of WFSs have been designed for AO systems, such as Shack-Hartmann WFS (SH-WFS). The WFS operator, which maps the incoming residual phase  $\phi^{\text{res}}(\cdot, t)$  to the WFS measurement, can be linear or nonlinear depending on the specific kind of the WFS. In this paper, we assume a linear relationship between the residual phase and the SH-WFS measurement.

Let us start from the continuous SH-WFS model, where the telescope aperture  $\Omega$  is divided into an array of small lenslets, so-called subapertures. The WFS is modeled as operator  $\Gamma : H^{11/6}(\Omega) \rightarrow \mathbb{R}^{n^2 \times 2}$  (cf., e.g., [16]) mapping a phase  $\phi^{\text{res}}(\mathbf{x}, t)$  onto measurements  $\mathbf{s}_t$  obtained on  $n \times n$  subapertures, i.e.,

$$\mathbf{s}_t = \Gamma \phi^{\text{res}}(\mathbf{x}, t).$$

These SH measurements  $\mathbf{s}_t$  are gradients averaged over the subapertures  $\Omega_{i,j}$ ,  $i, j = 1, \dots, n$ , with  $\cup_{i,j=1}^n \Omega_{i,j} = \Omega$ . **Note that for a general geometry of  $\Omega$ , e.g., a circle or a ring of subapertures, some  $\Omega_{i,j}$  might be not valid, i.e., there will be no measurements  $\mathbf{s}_{t,i,j}$ .** In order to compute the incoming phase and, therefore the necessary DM shape, the 2D function  $\phi^{\text{res}}(x, t)$  has to be reconstructed. However, the DM only has a finite number of actuators and thus it is sufficient to perform a discrete phase reconstruction instead of inverting the continuous operator. We view  $\Gamma$  as a combination of a projector  $P_n : H^{11/6}(\Omega) \rightarrow \mathbb{R}^{(n+1) \times (n+1)}$  and a discrete SH-WFS operator  $\Gamma_n : \mathbb{R}^{(n+1) \times (n+1)} \rightarrow \mathbb{R}^{n^2 \times 2}$ , i.e.,  $\Gamma = \Gamma_n P_n$ . Several ways to choose the  $(n+1) \times (n+1)$  grid exist and one possible choice is the so-called Fried geometry. In the Fried geometry, the telescope aperture is

divided into  $(n+1) \times (n+1)$  small squares  $\bar{\Omega}_{ij}$ , with  $\cup_{i,j} \bar{\Omega}_{i,j} = \Omega$ , and the corresponding pixel value  $a_{ij}$ ,  $i, j = 1, \dots, n+1$ , is calculated as the average of the incoming phase over this square, i.e.,

$$a_{ij} = \frac{1}{|\bar{\Omega}_{ij}|} \int_{\bar{\Omega}_{ij}} \phi(\mathbf{x}) d\mathbf{x}.$$

The discrete representation of the incoming phase can then be obtained as a solution  $\phi_t^{\text{res, coarse}}$  to the discrete inverse problem

$$\mathbf{s}_t = \Gamma_n \phi_t^{\text{res, coarse}} + \boldsymbol{\eta}_t, \quad (2)$$

where  $\phi_t^{\text{res, coarse}} := P_n \phi^{\text{res}}(x, t)$  and  $\boldsymbol{\eta}_t$ , models the noise.

Even though the above model is sufficient for AO control, we need additional operators for our high resolution approach as we want to reconstruct a phase in higher resolution. Let  $Q_{nm}$ , for  $k \in \mathbb{N}$  be the projector from  $H^{11/6}(\Omega)$  onto  $\mathbb{R}^{(nk+1) \times (nk+1)}$ ,  $R_k$  the refinement operator mapping a phase from  $\mathbb{R}^{(n+1) \times (n+1)}$  to  $\mathbb{R}^{(nk+1) \times (nk+1)}$  and  $C_k$  its related coarsening operator mapping a fine resolution phase from  $\mathbb{R}^{(nk+1) \times (nk+1)}$  to  $\mathbb{R}^{(n+1) \times (n+1)}$ . From this we can model the measurements of a higher resolution phase  $\phi_t^{\text{res}} := Q_{nk} \phi^{\text{res}}(x, t)$  as before as **should it be  $\mathbb{R}^{(nk+1) \times (nk+1)}$  or  $\mathbb{R}^{k(n+1) \times k(n+1)}$ ??**

$$\mathbf{s}_t = \Gamma_n C_k \phi_t^{\text{res}} + \boldsymbol{\eta}_t, \quad (3)$$

where  $\boldsymbol{\eta}_t$  models the noise. Note that the refinement and coarsening operator are not uniquely defined.

An illustration of the grids of the SH-WFS measurement and the high resolution residual phase is given in Figure 1a in which the SH-WFS measurement is considered to be located at the center of the subaperture following the Fried geometry [12].

When an AO system is running, the residual phase  $\phi^{\text{res}}(\mathbf{x}, t)$  is seen by the WFS and the next update for the DM is computed from the WFS measurements. Within this update process usually the motion of the atmosphere during the measurement and computation time is neglected due to the small shift and the coarse resolution of the WFS. To solve this problem several direct methods were developed and studied in simulation and on-sky [35, 25, 26, 22, 32, 1, 2]. However, to reconstruct a high resolution phase from multiple frames, the shift of the atmosphere has to be taken into account.

## 2.2 DM data as the measurement

One of the major tasks of a closed-loop AO system is finding an estimate of the residual phase  $\phi^{\text{res}}(\cdot, t)$  before applying the update of the DM shape at time  $t+1$ . However, a real time reconstruction method does not solve the problem (3) for  $\phi_t^{\text{res}}$ , but is limited by the resolution of the WFS measurement and the computation time. In fact, the inverse problem (2) is considered instead. From the solution of (2), the new DM shape  $\phi_{t+1}^{\text{DM}}$  is computed as

$$\phi_{t+1}^{\text{DM}} = \phi_t^{\text{DM}} + \alpha \cdot \phi_t^{\text{res, coarse}},$$

where  $\alpha > 0$  is the so-called loop gain and the initial DM shape  $\phi_{-1}^{\text{DM}} = 0$ . Figure 1b illustrates the discretization for the SH-WFS case. Let us denote the computed residual phase from the real time reconstruction method by  $\phi_t^{\text{res, coarse}}$ . As a solution to the coarse

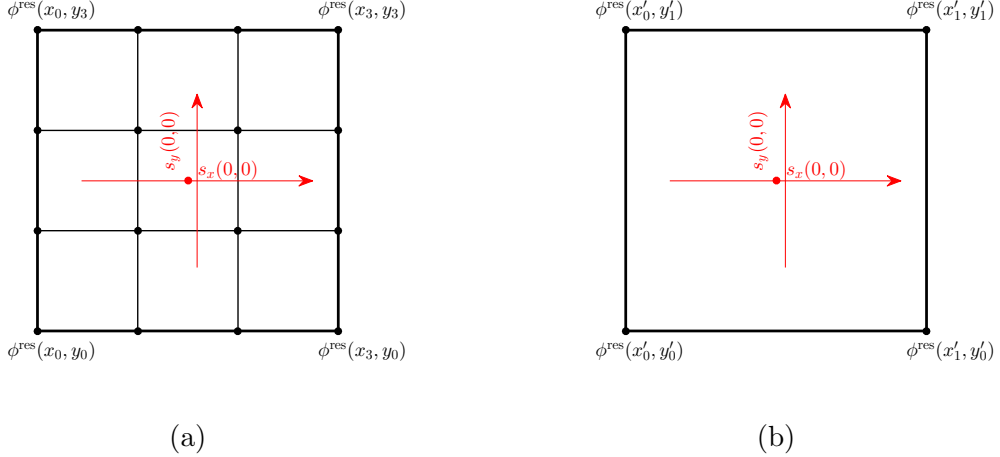


Figure 1: (a) The SH-WFS measurement and the high resolution residual phase in a subaperture of the WFS. The subaperture is bounded by the outermost square whose side length is 3 times the grid spacing of  $\phi^{\text{res}}$ ,  $(x_i, y_j)$  are the grid points. The measurement  $s_x(0,0)$  and  $s_y(0,0)$  is modeled as the average slope in the  $x$  direction and  $y$  direction in the subaperture respectively. (b) The SH-WFS measurement and the low resolution residual phase in a subaperture. In this example,  $(x'_i, y'_j)$  are the grid points which satisfy  $x'_i = x_{3i}, y'_j = y_{3j}$ .

grid problem (2),  $\phi_t^{\text{res, coarse}}$  has the same resolution as the WFS measurement. The grids of  $\phi_t^{\text{res, coarse}}$  and  $Q_{nm}\phi_t^{\text{res}}$  are compared in Figure 2a.

For a reconstruction of the high resolution residual phase  $\phi_t^{\text{res}}$ , one may start from the low resolution estimate  $\phi_t^{\text{res, coarse}}$  obtained by the reconstruction algorithm in the real time computer to adjust the DM. This means that  $\phi_t^{\text{res, coarse}}$  is treated as the input to our problem instead of  $\mathbf{s}_t$ . We note that this might be of interest for application in order to reduce the amount of stored data.

As the piston mode (i.e., the constant function) is always unseen by a SH-WFS,  $\phi_t^{\text{res, coarse}}$  is defined only up to an additive constant. In an individual time step, the additive constant is trivial as one may let  $\phi_t^{\text{res, coarse}}$  have zero mean without effecting the AO compensation. However, the additive constant in  $\phi_t^{\text{res, coarse}}$  should be taken into account in a post-processing step as the high resolution reconstruction of  $\phi_t^{\text{res}}$  depend on multiple time frames  $\{\phi_i^{\text{res, coarse}} \mid i = \dots, t-1, t, t+1, \dots\}$ , which may have non consistent constants. Motivated by this observation and equation (2), we compute a pseudo WFS measurement

$$\tilde{\mathbf{s}}_t := \Gamma_n \phi_t^{\text{res, coarse}}, \quad (4)$$

and use it as an approximation of  $\mathbf{s}_t$  in the model (3). Note that constants are always in the null space of  $\Gamma$  and  $\Gamma_n$ .

### 3 Estimating the residual phase in high resolution

Our approach is based on the observation model (3). The data we use is a sequence of coarse residual phases stored in the AO system. We assume that the DM actuators are located at the grid points of  $\phi_t^{\text{res, coarse}}$ . Through the so-called influence functions of the actuators the DM shape is known as a function on  $\mathbb{R}^2$ . Consequently, a discrete version

Table 1: Data for high resolution reconstruction

Data	Description
$\phi_t^{\text{res, coarse}}$	the computed phase residual on coarse grid at time $t$ , an estimate for $\phi^{\text{res}}(\mathbf{x}, t)$
$\tilde{\mathbf{s}}_t$	the pseudo WFS measurement given by (4)
$\tilde{\phi}_t^{\text{DM}}$	the high resolution DM shape at time $t$
$\mathbf{v}$	the wind velocity, which is constant over the aperture and time

$\tilde{\phi}_t^{\text{DM}}$  on the same grid as  $\phi^{\text{res}}$  is also available from  $\phi_t^{\text{DM}}$ . From the set of all DM shapes  $\phi_t^{\text{DM}}$  we can also find the computed residual phase  $\phi_t^{\text{res, coarse}}$  as it can be determined by  $\frac{1}{\alpha}(\phi_{t+1}^{\text{DM}} - \phi_t^{\text{DM}})$ .

To sum up, we start from the data given in Table 1 and we want to find an estimate of the high resolution residual phase  $\phi_t^{\text{res}}$ .

### 3.1 Taylor frozen flow hypothesis

In order to compute a highresolution phase, we make use of the Taylor frozen flow (TFF) hypothesis [27]: The atmospheric turbulence is composed of a number of layers located at different altitudes above the ground. Each of the layers does not change its shape on small time scales ( $t \in [0, T]$ ) and moves across the telescope aperture with a constant velocity due to wind. In a first step, we assume a one-layer model. As a consequence of the TFF hypothesis, the incoming phase reaching the telescope has a translational motion as

$$\phi(\mathbf{x}, t) = \phi(\mathbf{x} - \mathbf{v}t, 0), \quad (5)$$

where  $\mathbf{v} \in \mathbb{R}^2$  is the wind velocity and  $t \in [0, T]$  denotes the time. Equation (5) together with (1) implies that  $\phi(\mathbf{x}, 0)$  is measured repeatedly by the WFS, provided that the DM shapes  $\phi^{\text{DM}}(\mathbf{x}, t)$  are known. Based on this fact a high resolution reconstruction of  $\phi(\mathbf{x}, 0)$  is possible.

In order to use (5), we first assume for our model that the wind speed and direction are known from some exterior measurements. We define a discrete motion operator  $M_{\mathbf{v}, t}$  acting on  $\phi_t$  associated to the translation of the form  $f(\mathbf{x}) \rightarrow f(\mathbf{x} + t\mathbf{v})$ . Interpolation will be needed if the shift  $t\mathbf{v}$  is not a multiple of the grid spacing, as shown in Figure 2b. Throughout this paper, bilinear interpolations are employed for constructing  $M_{\mathbf{v}, t}$ . With the motion operator  $M_{\mathbf{v}, t}$ , equation (5) can be reformulated as

$$M_{\mathbf{v}, t}\phi_t \approx \phi_0, \quad (6)$$

which is not exact due to the interpolations. We assume that the precise value of the wind velocity is known at the moment and study the inexact wind velocity case later.

### 3.2 Turbulence statistics

The statistical properties of the atmospheric turbulence have been well studied. In Kolmogorov's theory, atmospheric turbulence is assumed to be a homogeneous and isotropic random process [19, 33]. The turbulence statistics are usually described by its power

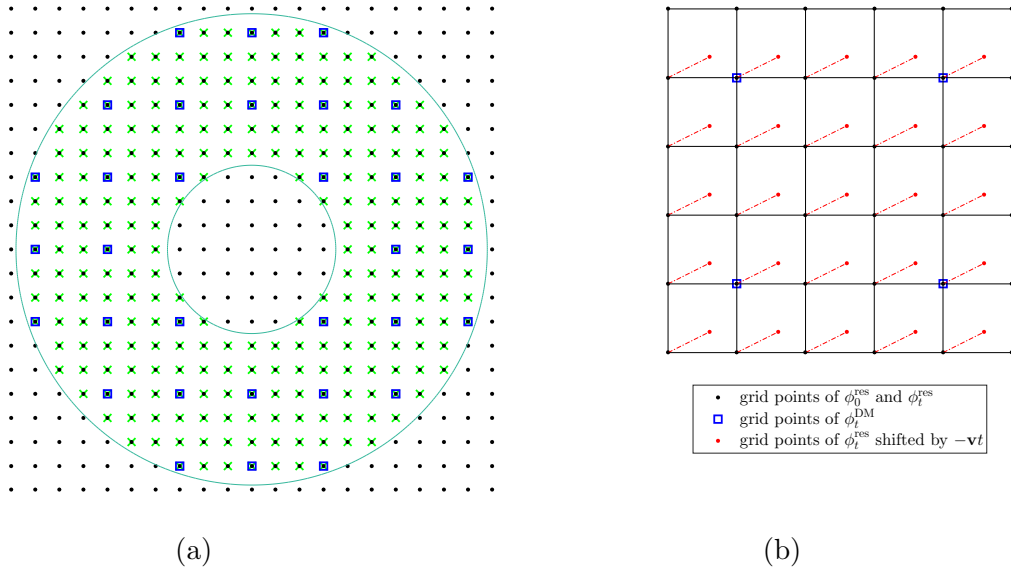


Figure 2: (a) three different discretization grids. The black dots, the blue square and the green cross represent the points on the grids of  $\phi_t$ ,  $\phi_t^{\text{res, coarse}}$  and  $\phi_t^{\text{res}}$ , respectively. In this example the grid of  $\phi_t^{\text{res}}$  is 3 times finer than that of  $\phi_t^{\text{res, coarse}}$ . The residual phase  $\phi_t^{\text{res}}$  and computed phase  $\phi_t^{\text{res, coarse}}$  lie on the annular aperture only. (b) The grid of  $\phi_t^{\text{res}}$  shifted by  $-\mathbf{v}t$  (i.e., the small red dots) does not fall on the grid of  $\phi_0^{\text{res}}$ . To define the discrete motion operator, the shifted  $\phi_t^{\text{res}}$  should be interpolated to the grid of  $\phi_0^{\text{res}}$  (i.e., the black dots).

spectral density (PSD) and there are various versions of PSDs in the literature. In this paper, we assume the von Karman PSD of the phase  $\phi(\mathbf{x})$  (see, e.g., [24]) given by

$$\mathcal{P}_\phi(\boldsymbol{\kappa}) = \frac{0.023r_0^{-5/3}}{(\kappa_0^2 + |\boldsymbol{\kappa}|^2)^{11/6}},$$

where  $r_0$  is the Fried parameter,  $\kappa_0 = 1/L_0$  and  $L_0$  is the atmospheric turbulence outer-scale. The covariance function of the phase is the inverse Fourier transform of the PSD, i.e.,

$$C_\phi = \mathcal{F}^{-1}(\mathcal{P}_\phi), \quad (7)$$

where  $\mathcal{F}$  denotes the Fourier transform.

In a discrete setting, the covariance matrix  $C_\phi$  derived from (7) and its inverse are dense and therefore not efficient in real computation especially for large scale problems. Many approximations of the covariance matrix have been developed in the past decades in order to achieve fast computations, see for instance [28, 34]. In particular, B. Ellerbroek showed in [9] that the biharmonic operator  $\Delta^2$  provides a good approximation to the inverse covariance operator. The discrete biharmonic operator has sparsity which contributes to efficient matrix-vector multiplications and shows great advantages when iterative solvers are applied.

### 3.3 High resolution reconstruction with known wind velocities

In the following, we will set up a functional which is minimized to obtain a high resolution reconstruction of the residual phase. We use the previously introduced operators

$\Gamma$ , which relates the two different discretization grids in (3), and  $M_{\mathbf{v},t}$ , which accounts for atmospheric motion due to wind in (6). As data, we use the set of pseudo WFS measurements  $\{\tilde{\mathbf{s}}_t\}$  to replace the set of WFS data  $\{\mathbf{s}_t\}$ . Therefore, the high resolution reconstruction does not require any AO data other than the DM shapes. Due to the fact that the number of high resolution pixels is bigger than the dimension of the measurements, the high resolution reconstruction problem is ill-posed. As in practice  $\tilde{\mathbf{s}}_t$  always contains noise from the sensor and the real time reconstruction algorithm, regularization techniques are necessary to reach an accurate and stable reconstruction. Additionally, we would like to use the statistics of the turbulence. To this end, let  $H_1 = H + \epsilon I$ , where  $H$  is the discrete Laplacian operator,  $\epsilon > 0$  and  $I$  the identity matrix. The matrix  $\epsilon I$  is an analogy to  $\kappa_0$  in  $\mathcal{P}_\phi$  and avoids zero eigenvalues appearing in  $H$ . Assuming the von Karman phase PSD,  $H_1^2$  approximates the inverse covariance matrix of  $\phi_t$  up to a scaling constant.

As the TFF hypothesis is valid for the incoming phase rather than the residual phase we first reconstruct  $\phi_t$  and then an estimate of  $\phi_t^{\text{res}}$  using

$$\phi_t^{\text{res}} = \phi_t - \tilde{\phi}_t^{\text{DM}},$$

which is a discrete version of (1). In summary, we adopt the following model for the reconstruction of the high resolution wavefront

$$\min_{\Phi} \mathcal{J}_0^\beta(\Phi) := \frac{1}{2} \sum_{t=0}^T \left( \left\| W\Gamma_n C_m \left( \phi_t - \tilde{\phi}_t^{\text{DM}} \right) - \tilde{\mathbf{s}}_t \right\|^2 + \beta \left\| H_1 \phi_t \right\|^2 \right), \quad (8)$$

$$\text{subject to } \phi_0 = M_{\mathbf{v},t} \phi_t, \quad t = 0, \dots, T,$$

where  $\Phi$  is the column stacking of  $\phi_0, \dots, \phi_T$ , and  $\beta$  is the regularization parameter that has to be chosen according to the noise level and the strength of the atmospheric turbulence. The matrix  $W$  defines the pupil mask. Note that the motion operator  $M_{\mathbf{v}}$  is known as  $\mathbf{v}$  is given.

Let us consider replacing  $H_1$  by the exact covariance matrix  $C_\phi^{-1/2}$  and impose the following conditions

- the noise  $\tilde{\boldsymbol{\eta}}_t := \tilde{\mathbf{s}}_t - W\Gamma\phi_t^{\text{res}}$  is white Gaussian,
- $\phi_t$  is a realization of Gaussian random variables with covariance matrix  $C_\phi$  and zero mean,
- the regularization parameter  $\beta$  is properly chosen,
- the wind velocity  $\mathbf{v}$  satisfies that the components of  $\mathbf{v}t$  are multiples of the grid spacing,

then the solution to our model can be interpreted as the conditional mean (CM) or the minimum mean squared error (MMSE) estimate under the Bayesian framework. The corresponding minimizer in this case is also known as the maximum a posteriori (MAP) estimate.

### 3.4 Adaptive wind velocities

Having available only an estimate for the wind velocity  $\mathbf{v}$ , denoted by  $\mathbf{v}^{(0)}$ , we need to modify the model such that it allows variation of this estimate. For imprecise information on wind speed and direction, the associated motion operator, denoted by  $M_{\mathbf{v}^{(0)},t}$ , becomes imprecise. The model in (8) relies on the assumption that

$$\phi_0 - M_{\mathbf{v}^{(0)},t} \phi_t \approx 0,$$

which does not hold when  $\mathbf{v}^{(0)}$  is not close enough to  $\mathbf{v}$  and  $|t|$  is big, due to the resulting cumulative error in the motion operator  $M_{\mathbf{v}^{(0)},t}$ . In this case, an approximation based on the successive difference

$$M_{\mathbf{v}^{(0)},t}\boldsymbol{\phi}_t - M_{\mathbf{v}^{(0)},t+1}\boldsymbol{\phi}_{t+1} \approx 0,$$

is more reliable.

Furthermore, in order to preserve the consistency between the (pseudo) measurement and the TFF hypothesis with given wind velocity which is not accurate enough, the wind velocity is considered as a variable in the functional. Therefore, it can be adjusted appropriately during the minimization process.

In summary, we solve the joint minimization problem for both an estimated high resolution phase and an estimated wind velocity

$$\begin{aligned} \min_{\Phi, \mathbf{v}} \mathcal{J}_1^\beta(\Phi, \mathbf{v}) &:= \frac{1}{2} \sum_{t=0}^T \left( \left\| W\Gamma_n C_m \left( \boldsymbol{\phi}_t - \tilde{\boldsymbol{\phi}}_t^{\text{DM}} \right) - \tilde{\mathbf{s}}_t \right\|^2 + \beta \|H_1 \boldsymbol{\phi}_t\|^2 \right), \\ \text{subject to } M_{\mathbf{v},t}\boldsymbol{\phi}_t &= M_{\mathbf{v},t+1}\boldsymbol{\phi}_{t+1}, \quad t = 0, \dots, T-1. \end{aligned} \quad (9)$$

### 3.5 The atmospheric tomography problem

Up to now we focused on the incoming phase  $\boldsymbol{\phi}(\mathbf{x}, t)$  yielded by one single thin atmospheric turbulence layer. In a more realistic situation, the distorted phase  $\boldsymbol{\phi}(\mathbf{x}, t)$  is a result of the 3D atmospheric turbulence. It is commonly considered that the distortions only happen at some discrete heights in the Earth's atmosphere (see, e.g., [24]). In such a setting, the incoming phase is a projection of the phase distortions at these layers, i.e.,

$$\boldsymbol{\phi}(\mathbf{x}, t) = \sum_{l=1}^L \boldsymbol{\phi}_l(\mathbf{x}, t), \quad (10)$$

where  $\boldsymbol{\phi}_l(\mathbf{x}, t)$  is the distortion of the phase corresponding to the  $l^{\text{th}}$  layer and  $L$  is the number of layers. Assuming the distortions of the phases  $\boldsymbol{\phi}_l$  are independent of each other, the translational motion is valid on each layer, i.e.,

$$\boldsymbol{\phi}_l(\mathbf{x}, t) = \boldsymbol{\phi}_l(\mathbf{x} - \mathbf{v}_l t, 0), \quad (11)$$

in which  $\mathbf{v}_l \in \mathbb{R}^2$  is the wind velocity of the  $l^{\text{th}}$  layer. If  $\mathbf{v}_1, \dots, \mathbf{v}_L$  are different, then  $\boldsymbol{\phi}(\cdot, t)$  does not preserve its form as  $t$  changes, i.e., (5) does not hold. Our idea to obtain a high resolution incoming phase is first reconstructing  $\boldsymbol{\phi}_l(\mathbf{x}, t)$  in high resolution with the TFF hypothesis (11), and then doing projections to get  $\boldsymbol{\phi}(\mathbf{x}, t)$  according to equation (10). Note that this results in a tomography problem as in an AO system only information about  $\boldsymbol{\phi}(\mathbf{x}, t)$  is available. Figure 3a displays an example of the tomography problem in a 3-layer setting. Unfortunately, with some uncertainty in the wind velocities, the exact unknown-to-data operator is unavailable. Small perturbations on the operator due to the errors in the wind velocities are illustrated in Figure 3b.

Let  $\boldsymbol{\phi}_{l,t}$  denote a discrete version of  $\boldsymbol{\phi}_l(x, t)$  in high resolution and  $\Phi$  be a concatenation of  $\boldsymbol{\phi}_{1,0}, \boldsymbol{\phi}_{1,1}, \dots, \boldsymbol{\phi}_{L,T}$ . As a direct extension of the previous model, we consider the following optimization problem

$$\begin{aligned} \min_{\Phi, \mathbf{v}} \mathcal{J}_2^\beta(\Phi, \mathbf{v}) &:= \frac{1}{2} \sum_{t=0}^T \left( \left\| W\Gamma_n C_m \left( \sum_{l=1}^L \boldsymbol{\phi}_{l,t} - \tilde{\boldsymbol{\phi}}_t^{\text{DM}} \right) - \tilde{\mathbf{s}}_t \right\|^2 + \beta \sum_{l=1}^L \|H_l \boldsymbol{\phi}_{l,t}\|^2 \right), \\ \text{subject to } M_{\mathbf{v}_l,t}\boldsymbol{\phi}_{l,t} &= M_{\mathbf{v}_l,t+1}\boldsymbol{\phi}_{l,t+1}, \quad t = 0, \dots, T-1, \quad l = 1, 2, \dots, L, \end{aligned} \quad (12)$$

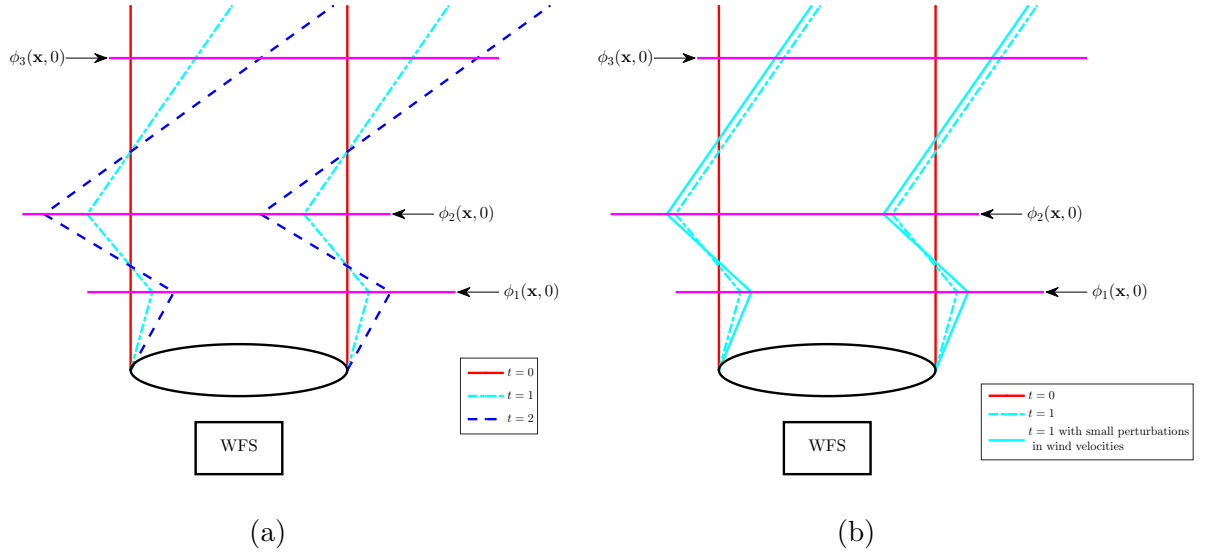


Figure 3: (a) The tomography problem in a 3-layer case. The winds of the layers shift the observed area of the distorted phase with the time, as illustrated by the bended paths corresponding to  $t = 1$  and  $t = 2$ . (b) The path is perturbed by the inexact wind velocity, resulting in an inaccurate tomography operator.

where  $\mathbf{v}$  is a column stacking of  $\mathbf{v}_1, \dots, \mathbf{v}_L$ ,  $H_l = \frac{1}{c_l} (H + \epsilon I)$  and  $\sum_{l=1}^L c_l^2 = 1$ , where  $c_l^2$  are the so-called  $c_n^2$ -values of the atmospheric layers (see Section 5.1). Once the minimizer of (12), denoted by  $(\{\hat{\phi}_{l,t}\}, \hat{\mathbf{v}})$ , is obtained, the residual phase  $\phi_t^{\text{res}}$  is estimated as  $\sum_{l=1}^L \hat{\phi}_{l,t} - \tilde{\phi}_t^{\text{DM}}$  according to equations (10) and (1).

## 4 Numerical Minimization

A numerical minimization procedure is needed to compute the estimate  $\phi_t^{\text{res}}$  from (9) or, respectively, (12). Let us consider the one-layer case (9) first. It is clear that the optimization problem is not convex as the constraints are not convex functions in  $\mathbf{v}$ . To deal with such a problem, we implement an alternating direction method to find a minimizer of the objective function with respect to  $\Phi$  and  $\mathbf{v}$ .

We define  $M_{\mathbf{v}}$  and  $\tilde{M}_{\mathbf{v}}$  as the block matrices of the form

$$M_{\mathbf{v}} = \begin{bmatrix} M_{\mathbf{v},0} & & & \\ & \ddots & & \\ & & M_{\mathbf{v},T-1} & 0 \end{bmatrix}, \quad \tilde{M}_{\mathbf{v}} = \begin{bmatrix} 0 & M_{\mathbf{v},1} & & \\ & & \ddots & \\ & & & M_{\mathbf{v},T} \end{bmatrix},$$

and let  $A_{\mathbf{v}} = M_{\mathbf{v}}^T (\tilde{M}_{\mathbf{v}} - M_{\mathbf{v}})$ , where the superscript  $T$  denotes the transpose of a matrix. Then the constraint in (9) can be equivalently written as  $A_{\mathbf{v}} \Phi = 0$ . The corresponding augmented Lagrangian functional is given by

$$\mathcal{L}_1(\Phi, \mathbf{v}, \boldsymbol{\lambda}) = \mathcal{J}_1^\beta(\Phi, \mathbf{v}) + \boldsymbol{\lambda}^* A_{\mathbf{v}} \Phi + \frac{\tau}{2} \|A_{\mathbf{v}} \Phi\|^2,$$

in which  $\tau \geq 0$  is the augmented Lagrangian parameter (see, e.g., [3]). Starting from  $\mathbf{v} = \mathbf{v}^{(0)}$ , an alternating update on  $\Phi$ ,  $\mathbf{v}$  and  $\boldsymbol{\lambda}$  leads to estimates of the phase and wind

velocities. To be specific, the method requires solving the following two subproblems alternatively

$$\Phi^{(k+1)} = \arg \min_{\Phi} \left( \mathcal{J}_1^\beta(\Phi, \mathbf{v}^{(k)}) + \frac{\tau}{2} \left\| A_{\mathbf{v}^{(k)}} \Phi + \frac{\boldsymbol{\lambda}^{(k)}}{\tau} \right\|^2 \right), \quad (13)$$

$$\mathbf{v}^{(k+1)} = \arg \min_{\mathbf{v}} \frac{\tau}{2} \left\| A_{\mathbf{v}} \Phi^{(k+1)} + \frac{\boldsymbol{\lambda}^{(k)}}{\tau} \right\|^2. \quad (14)$$

with  $\boldsymbol{\lambda}^{(k)}$  being updated as

$$\boldsymbol{\lambda}^{(k+1)} = \boldsymbol{\lambda}^{(k)} + \tau A_{\mathbf{v}^{(k+1)}} \Phi^{(k+1)}. \quad (15)$$

The subproblem (13) is a least squares problem, the solution of which is obtained by solving a linear system. The second subproblem (14) is more difficult as it is neither linear nor convex. We will show that it is related to an image registration problem and the optical flow algorithm proposed by Gilliam et al. [14, 13] can be adapted for finding a good approximation to the solution.

#### 4.1 All-pass filters for wind estimation

First, we consider the explicit objective function of subproblem (14), i.e.,

$$\left\| A_{\mathbf{v}} \Phi^{(k+1)} + \frac{\boldsymbol{\lambda}^{(k)}}{\tau} \right\|^2 = \sum_{t=0}^{T-1} \left\| M_{\mathbf{v},t}^T M_{\mathbf{v},t+1} \boldsymbol{\phi}_{t+1}^{(k+1)} - M_{\mathbf{v},t}^T M_{\mathbf{v},t} \boldsymbol{\phi}_t^{(k+1)} + \boldsymbol{\lambda}_t^{(k)} / \tau \right\|^2.$$

To simplify notations, let  $\mathbf{p}_{\mathbf{v},t} := M_{\mathbf{v},t}^T M_{\mathbf{v},t+1} \boldsymbol{\phi}_{t+1}$  and  $\mathbf{q}_{\mathbf{v},t} := M_{\mathbf{v},t}^T M_{\mathbf{v},t} \boldsymbol{\phi}_t$ , and  $\mathbf{v} := \mathbf{v}^{(k)} + \mathbf{u}$ . In the frequency domain, for any displacement vector  $\mathbf{u} = [u_1, u_2]^T$ ,

$$\begin{aligned} \widehat{\mathbf{p}}_{\mathbf{v}^{(k)}+\mathbf{u},t} &\approx [e^{i(\omega_1 u_1 + \omega_2 u_2)}]_{\boldsymbol{\omega}} \circ \widehat{\mathbf{p}}_{\mathbf{v}^{(k)},t}, \\ \widehat{\mathbf{q}}_{\mathbf{v}^{(k)}+\mathbf{u},t} &\approx \widehat{\mathbf{q}}_{\mathbf{v}^{(k)},t}, \end{aligned} \quad (16)$$

where  $\boldsymbol{\omega} = [\omega_1, \omega_2]^T$ ,  $\circ$  denotes the Hadamard product and  $\widehat{\mathbf{p}}_{\mathbf{v},t}$  the Fourier transform of  $\mathbf{p}_{\mathbf{v},t}$ . It is clear that the filter  $[e^{i(\omega_1 u_1 + \omega_2 u_2)}]_{\boldsymbol{\omega}}$  is an all pass filter. Equation (16) implies that

$$\begin{aligned} \left\| A_{\mathbf{v}^{(k)}+\mathbf{u}} \Phi + \frac{\boldsymbol{\lambda}}{\tau} \right\|^2 &\approx \sum_{t=0}^{T-1} \left\| [e^{i(\omega_1 u_1 + \omega_2 u_2)}]_{\boldsymbol{\omega}} \circ \widehat{\mathbf{p}}_{\mathbf{v}^{(k)},t} - \widehat{\mathbf{q}}_{\mathbf{v}^{(k)},t} + \widehat{\boldsymbol{\lambda}}_t^{(k)} / \tau \right\|^2 \\ &= \sum_{t=0}^{T-1} \left\| [e^{i\frac{\omega_1 u_1 + \omega_2 u_2}{2}}]_{\boldsymbol{\omega}} \circ \widehat{\mathbf{p}}_{\mathbf{v}^{(k)},t} - [e^{-i\frac{\omega_1 u_1 + \omega_2 u_2}{2}}]_{\boldsymbol{\omega}} \circ \left( \widehat{\mathbf{q}}_{\mathbf{v}^{(k)},t} - \widehat{\boldsymbol{\lambda}}_t^{(k)} / \tau \right) \right\|^2 \\ &:= \sum_{t=0}^{T-1} \left\| [\widehat{f}(\omega_1, \omega_2)]_{\boldsymbol{\omega}} \circ \widehat{\mathbf{p}}_{\mathbf{v}^{(k)},t} - [\widehat{f}(-\omega_1, -\omega_2)]_{\boldsymbol{\omega}} \circ \left( \widehat{\mathbf{q}}_{\mathbf{v}^{(k)},t} - \widehat{\boldsymbol{\lambda}}_t^{(k)} / \tau \right) \right\|^2. \end{aligned} \quad (17)$$

The problem is converted into registering  $\mathbf{p}_{\mathbf{v}^{(k)},t}$  and  $\mathbf{q}_{\mathbf{v}^{(k)},t} - \boldsymbol{\lambda}_t^{(k)} / \tau$  for all  $t$  simultaneously. The last equality of (17) expresses the shifting motion by  $\mathbf{u}$  in a forward-backward form and later we will show that such an expression is crucial in constructing an all pass filter like  $[e^{i(\omega_1 u_1 + \omega_2 u_2)}]_{\boldsymbol{\omega}}$ .

The LAP algorithm proposed by Gilliam et al. [13] is based on a linear approximation of the filter  $f$  with a filter basis  $\{f_j\}_j$ . In particular, the filter basis is chosen as

$$\begin{aligned} f_0(x_1, x_2) &= \exp\left(-\frac{x_1^2 + x_2^2}{2\xi^2}\right), \\ f_1(x_1, x_2) &= x_1 f_0(x_1, x_2), \\ f_2(x_1, x_2) &= x_2 f_0(x_1, x_2). \end{aligned}$$

A larger basis is possible, but here we consider only the 3-dimensional case. To compute the  $\mathbf{u}^{(k)}$  that minimizes the last term of (17), the LAP algorithm first searches for the filter  $f$  that is approximated by  $\sum_{j=0}^2 k_j f_j(x_1, x_2)$ , where  $k_j$  are the minimizer of

$$\min_{\{k_j\}} \sum_{t=0}^{T-1} \left\| \left[ \sum_{j=0}^2 k_j f_j(x_1, x_2) \right] * \mathbf{p}_{\mathbf{v}^{(k)}, t} - \left[ \sum_{j=0}^2 k_j f_j(-x_1, -x_2) \right] * \left( \mathbf{q}_{\mathbf{v}^{(k)}, t} - \boldsymbol{\lambda}_t^{(k)} / \tau \right) \right\|^2, \quad (18)$$

in which  $*$  denotes the convolution operation. This can be done by solving a small linear system in  $[k_0, k_1, k_2]^T$ . Note that

$$\left[ \frac{\sum_{j=0}^2 k_j \widehat{f}_j(\omega_1, \omega_2)}{\sum_{j=0}^2 k_j \widehat{f}_j(-\omega_1, -\omega_2)} \right]_{\omega}$$

is also an all pass filter. Finally, the solution  $\mathbf{u}^{(k)}$  is computed as

$$u_1^{(k)} = 2 \frac{\sum_{x_1} \sum_{j=0}^2 x_1 k_j f_j(x_1, x_2)}{\sum_{j=0}^2 k_j f_j(x_1, x_2)} \quad \text{and} \quad u_2^{(k)} = 2 \frac{\sum_{x_2} \sum_{j=0}^2 x_2 k_j f_j(x_1, x_2)}{\sum_{j=0}^2 k_j f_j(x_1, x_2)}. \quad (19)$$

The above method is a simplified version of the LAP algorithm, as the original LAP algorithm is designed to compute a motion field, i.e.,  $\mathbf{u}$  is a vector field rather than a constant vector. To do this, the algorithm computes the velocity for each pixel by restricting the problem in a small window centered at the pixel under the assumption that the motion field within each window is nearly constant. However, in our problem we assume a constant velocity and hence it is computed using the entire domain.

## 4.2 The alternating direction method

In summary, the minimization process (14) results in a self-adaptive algorithm which updates the inexact wind velocity with the information from the observed data based on an implicit use of the TFF hypothesis. The algorithm is described in Algorithm I.

---

**Algorithm I**


---

**Input:**  $\phi_t^{\text{DM}}$  for  $t = 0, \dots, T$ ,  $\mathbf{v}^{(0)}$

**Output:** Estimates of residual phases  $\hat{\phi}_0^{\text{res}}, \dots, \hat{\phi}_T^{\text{res}}$  and the estimated wind velocity  $\hat{\mathbf{v}}$ .

Step 1. Initialization.

1. recover  $\phi_t^{\text{res, coarse}}$  from the DM data  $\phi_t^{\text{DM}}$ ,
2. compute the high resolution DM shape  $\tilde{\phi}_t^{\text{DM}}$  from  $\phi_t^{\text{DM}}$ ,
3. compute the pseudo WFS measurement  $\tilde{\mathbf{s}}_t$  with  $\phi_t^{\text{res, coarse}}$  by (4),
4. set  $\boldsymbol{\lambda}^{(0)} = 0$ .

Step 2. For  $k = 1, 2, \dots, m$ , repeat:

1. Compute  $\Phi^{(k)}$  as minimizer of the Lagrangian functional

$$\mathcal{J}_1^\beta(\Phi, \mathbf{v}^{(k-1)}) + (\boldsymbol{\lambda}^{(k-1)})^* A_{\mathbf{v}^{(k-1)}} \Phi + \frac{\tau}{2} \|A_{\mathbf{v}^{(k-1)}} \Phi\|^2,$$

over all  $\Phi$ . Here  $\Phi^{(k)}$  is a column stacking of  $\phi_0^{(k)}, \dots, \phi_T^{(k)}$ .

2. Estimate the wind velocity  $\mathbf{v}^{(k)} = \mathbf{v}^{(k-1)} + \mathbf{u}^{(k)}$  where  $\mathbf{u}^{(k)}$  is given by (19).
3.  $\boldsymbol{\lambda}^{(k)} = \boldsymbol{\lambda}^{(k-1)} + \tau A_{\mathbf{v}^{(k)}} \Phi^{(k)}$ .

Step 3. The output is given by  $\hat{\phi}_0^{\text{res}} = \phi_0^{(m)} - \tilde{\phi}_0^{\text{DM}}, \dots, \hat{\phi}_T^{\text{res}} = \phi_T^{(m)} - \tilde{\phi}_T^{\text{DM}}, \hat{\mathbf{v}} = \mathbf{v}^{(m)}$ .

---

Note that Algorithm I is not an exact alternating direction method of multipliers (see, e.g., [3]) as the optimization problem has a nonlinear constraint and the subproblem in  $\mathbf{v}$  is linearized as in (18). In real application, only values of  $\phi_t$  on the telescope aperture are useful. Although in our model  $\phi_t$  can be defined on a domain that is much bigger than the telescope aperture, it is not necessary to do so as the part outside the telescope aperture does not contribute to the blur of the observed image. For computational reasons,  $\phi_t$  is defined on a grid in a small rectangular domain covering the telescope aperture.

### 4.3 Solving the tomography problem

Let us now consider problem (12) which is also nonconvex. We introduce an algorithm similar to Algorithm I for the minimization.

We define  $A_{\mathbf{v}}$  as a block diagonal matrix with diagonal blocks  $A_{\mathbf{v}_1}, A_{\mathbf{v}_2}, \dots, A_{\mathbf{v}_L}$ . Then the equality constraints in (12) have a compact form  $A_{\mathbf{v}} \Phi = 0$ . The corresponding augmented Lagrangian functional is given by

$$\mathcal{L}_2(\Phi, \mathbf{v}, \boldsymbol{\lambda}) = \mathcal{J}_2^\beta(\Phi, \mathbf{v}) + \boldsymbol{\lambda}^* A_{\mathbf{v}} \Phi + \frac{\tau}{2} \|A_{\mathbf{v}} \Phi\|^2.$$

Again, the idea of updating  $\Phi, \mathbf{v}, \boldsymbol{\lambda}$  alternatively can be applied, and the main difficulty remains in the subproblem of minimizing  $\mathcal{L}_2$  with respect to  $\mathbf{v}$ . For fixed  $\Phi^{(k)}$  and  $\boldsymbol{\lambda}^{(k)}$ , the subproblem can be decomposed into

$$\min_{\mathbf{v}_i} \frac{\tau}{2} \left\| A_{\mathbf{v}_i} \Phi_i^{(k+1)} + \frac{\boldsymbol{\lambda}_i^{(k)}}{\tau} \right\|^2, \quad i = 1, \dots, L, \quad (20)$$

where  $\Phi_i^{(k+1)}$  and  $\boldsymbol{\lambda}_i^{(k)}$  are subvectors of  $\Phi^{(k+1)}$  and  $\boldsymbol{\lambda}^{(k)}$  corresponding to the  $i^{\text{th}}$  layer,  $i = 1, 2, \dots, L$ . The problem (20) has the same form as (14), which means that the update of  $\mathbf{v}$  can be performed in a layer-by-layer manner using the technique described

in Subsection 4.1. We use the update rule for  $\boldsymbol{\lambda}$  from (15). The resulting method is summarized in Algorithm II.

---

Algorithm II

---

**Input:**  $\phi_t^{\text{DM}}$  for  $t = 0, \dots, T$ ,  $\mathbf{v}^{(0)}$

**Output:** Estimates of residual phases  $\hat{\phi}_0^{\text{res}}, \dots, \hat{\phi}_T^{\text{res}}$  and the estimated wind velocity  $\hat{\mathbf{v}}$ .

Step 1. Initialization.

1. recover  $\phi_t^{\text{res, coarse}}$  from the DM data  $\phi_t^{\text{DM}}$ ,
2. compute the high resolution DM shape  $\tilde{\phi}_t^{\text{DM}}$  from  $\phi_t^{\text{DM}}$ ,
3. compute the pseudo WFS measurement  $\tilde{\mathbf{s}}_t$  of  $\phi_t^{\text{res, coarse}}$  by (4),
4. set  $\boldsymbol{\lambda}^{(0)} = 0$ .

Step 2. For  $k = 1, 2, \dots, m$ , repeat:

1. Compute  $\phi_{1,0}^{(k)}, \dots, \phi_{1,T}^{(k)}, \dots, \phi_{L,0}^{(k)}, \dots, \phi_{L,T}^{(k)}$  as a minimizer of the Lagrangian functional

$$\mathcal{J}_2^\beta(\Phi, \mathbf{v}^{(k-1)}) + (\boldsymbol{\lambda}^{(k-1)})^* A_{\mathbf{v}^{(k-1)}} \Phi + \frac{\tau}{2} \|A_{\mathbf{v}^{(k-1)}} \Phi\|^2,$$

over all  $\Phi$ . Concatenate the vectors  $\phi_{1,0}^{(k)}, \dots, \phi_{1,T}^{(k)}, \dots, \phi_{L,0}^{(k)}, \dots, \phi_{L,T}^{(k)}$  as  $\Phi^{(k)}$ .

2. For  $l = 1, 2, \dots, L$ , compute the new estimated the wind velocity at the  $l^{\text{th}}$  layer as

$$\mathbf{v}_l^{(k)} = \mathbf{v}_l^{(k-1)} + \mathbf{u}_l^{(k)}$$

where  $\mathbf{u}_l^{(k)}$  is given by (19).

3.  $\boldsymbol{\lambda}^{(k)} = \boldsymbol{\lambda}^{(k-1)} + \tau A_{\mathbf{v}^{(k)}} \Phi^{(k)}$ .

Step 3. The output is computed as  $\hat{\phi}_0^{\text{res}} = \sum_{l=1}^L \phi_{l,0}^{(m)} - \tilde{\phi}_0^{\text{DM}}, \dots, \hat{\phi}_T^{\text{res}} = \sum_{l=1}^L \phi_{l,T}^{(m)} - \tilde{\phi}_T^{\text{DM}}$ ,  $\hat{\mathbf{v}} = \mathbf{v}^{(m)}$ .

---

## 5 Simulation results

In order to validate our algorithm, we used a MATLAB-based AO simulation tool to obtain the required data. As benefit in simulation, we can compare the phase recovered on a fine grid to the true incoming phase.

### 5.1 Simulation setting

The simulated system is an SCAO system on an 8 m telescope, equipped with one  $40 \times 40$  Shack-Hartmann WFS, described in Table 2. We perform simulations for different atmospheric settings to demonstrate the power of our method. As starting point, we consider an atmosphere consisting just of one layer with a wind speed of 15 m/s in direction  $0^\circ$ . In the next steps, first we change the direction to  $30^\circ$  and second, we move to a two layer profile, with relative strengths 0.65 and 0.35. The altitudes of the layers are 0 and 5000 m, the wind speeds 15 m/s and the directions  $0^\circ$  and  $90^\circ$ , respectively.

As a last step, we take an atmospheric profile with 9 layers, often referred to as *ESO-standard profile* from [20]. This model is based on measurements at ESO's site Paranal in the Atacama desert with a Fried parameter  $r_0 = 12.9$  cm. In Table 3, the values for the 9-layer medium seeing atmosphere are given.

Telescope diameter	8 m
central obstruction	2.2 m
1 NGS Shack-Hartmann WFS	40 × 40 subapertures
WFS wavelength $\lambda$	0.589 $\mu\text{m}$
WFS integration time	2 ms
1 DM at height 0 m	closed loop
DM actuator spacing	0.2 m

Table 2: Description of the simulated SCAO system.

Layer	1	2	3	4	5	6	7	8	9
Height(m)	47	140	281	562	1125	2250	4500	9000	18000
$c_n^2$ -profile	0.522	0.026	0.044	0.116	0.098	0.029	0.059	0.043	0.06
wind speed	15	13	13	9	9	15	25	40	21
direction	0	$\pi/2$	$\pi$	$3\pi/2$	0	$\pi/2$	$\pi$	$3\pi/2$	0

Table 3: 9-layer median atmosphere.

The AO loop is controlled using the CuReD algorithm [25, 26] with optimized loop gain. We take the first 20 frames of an AO simulation using these parameters to show the performance of our algorithm.

Note that using more than 20 frames might improve the results further, however also clearly increases the computational costs. The maximum number of frames that can be used is related to the wind speed. If the atmospheric turbulence seen in the first frame is blown over the whole telescope and no part of it can be seen anymore in the  $T$ -th frame, it is reasonable to stop taking into account any frame after  $T$  steps. Note that therefore it is required that the frozen flow hypothesis holds for at least  $T$  frames. For the setting of Table 2 and a wind speed of 15 m/s, we have  $T = 267$ . However, one may also think of reconstructing the atmosphere on an ever bigger domain, and thus take into account more than  $T$  frames. In real observations this idea will most likely fail as the TFF hypothesis will not hold for 267 frames being equivalent to more than 0.5 s of real time. Therefore, we did not follow this idea further as it also increases the computational costs.

## 5.2 Numerical considerations

The residual of the incoming phase  $\phi^{\text{res}}(\mathbf{x}, t)$  is computed by the simulation software on a fine level with  $400 \times 400$  pixels across the telescope aperture, translating into 2 cm/pixel. The Shack-Hartmann WFS has  $40 \times 40$  subapertures and the DM  $41 \times 41$  actuators, which limits the resolution of the reconstructed incoming phase for usual AO control algorithm to this level as the DM cannot use higher resolved incoming phases.

Our method is able to provide a high resolution reconstruction, however we cannot choose it arbitrarily large as the resolution of the reconstruction should still be smaller than the resolution of the simulated incoming phase, in order to avoid an inverse crime. In the following simulations, the underlying grid for the high resolution reconstruction is chosen to be four times finer than the grid of the DM actuators, resulting in a  $161 \times 161$  reconstruction.

To judge the quality of our fine resolution reconstruction, we compare it to the ground truth. As a quality criterion, we take the  $l_2$ -norms of the reconstruction error, i.e.,

$$\|\hat{\phi}_t^{\text{res}} - \phi_t^{\text{res}}\|_2, \quad (21)$$

where  $t$  indicates the time step and  $\hat{\phi}_t^{\text{res}}$  is the result of our algorithm. Due to the different resolutions, we have to interpolate the simulated  $\phi^{\text{res}}(\cdot, t)$  to the same grid as  $\hat{\phi}_t^{\text{res}}$ . For this purpose, we use the MATLAB-function *interp2*. To make a comparison, we also interpolate  $\phi_t^{\text{res, coarse}}$  to the same grid as  $\hat{\phi}_t^{\text{res}}$  and compute the corresponding  $l_2$ -error. Since only the part of the phase inside the telescope aperture contributes to the image quality, in equation (21),  $\hat{\phi}_t^{\text{res}}$  and  $\phi_t^{\text{res}}$  are restricted to the telescope domain with the piston mode removed.

### 5.3 Numerical results

In this section we present the numerical results from several test runs. We always use the first 20 frames for our algorithm to compute the high resolution residual phase. We will demonstrate the performance of our algorithm by first assuming that exact wind velocities are given and solving problem (8). After that, we consider the situation where the exact values of wind velocities are unavailable which usually happens in real applications. Algorithm I and II with adaptive wind velocities are employed to find the high resolution reconstructions in this case.

#### 5.3.1 Exact wind velocity case

To highlight the strength of our method, we start with the simplest possible case, i.e., simulation 1: all atmospheric turbulence is located in one layer close to the ground, with known wind speed and direction, and a bright star can be used as a guide star. In this case the used AO control algorithm provides a correction in K-band close to the diffraction limit. Using our model (8), we can still reduce the  $l_2$ -error between the true residual phase  $\phi_t^{\text{res}}$  and the reconstructed residual phase  $\phi_t^{\text{res, coarse}}$  by 15 to 20%, see Figure 4a. The  $l_2$ -error of bilinear interpolation at the first time step is much bigger than the others because the control loop of the system has to be closed and no other information of the phase is available at this time within the AO control algorithm. Our high resolution reconstruction still results in a small  $l_2$ -error at the first time step since we have used the data from the following time steps as well. The  $l_2$ -error curve of our reconstruction has significantly less oscillation over the time than the  $l_2$ -error curve of the bilinear interpolation, which is reasonable as our reconstructed phase does not rely heavily on data of a specific time step and hence prevents enormous errors.

As a next step, in simulation 2, we change the guide star flux to simulate a faint star. This leads to a decreased correction quality through the AO control algorithm but leaves more room for improvement of the reconstructed residual phase. With low flux the real time reconstruction for the adaptive system has correction errors that are bigger than the reconstruction with high flux. So for the low flux case, the AO system is unable to use the data efficiently enough, and we expect that a more significant improvement can be made by our algorithm which takes full consideration of the relation of the data from all time steps. Indeed, our method reduces the residual  $l_2$ -error by 70 to 80%, as shown in Figure 4b.

In the first two simulations the wind direction was parallel to an axis, which gives more information for high resolution reconstruction in one direction than in the other. The best possible situation would be a wind direction of  $45^\circ$  to the axes, leading to an equally spread gain of information in x- and y-direction. However, such a direction might not occur in practice, thus we choose an angle of  $30^\circ$  with respect to the first axis for simulation 3. Changing again to high flux, even in this case our algorithm gives an improvement of 45% to 65%, shown in Figure 4c. Compared to the accuracy improvement for simulation 1 (which is around 20%), the improvement for this one is much more significant. However, this is reasonable as the sampling points from different time steps have less overlap. Recall that the angle between the wind velocity and the first axis is  $30^\circ$ , which ensures that the trajectories of coarse grid points do not have overlap with each other. In simulation 1, in contrast, the coarse grid points always fall in  $n + 1$  lines parallel to the first axis where  $n$  is the number of grid point on the second axis.

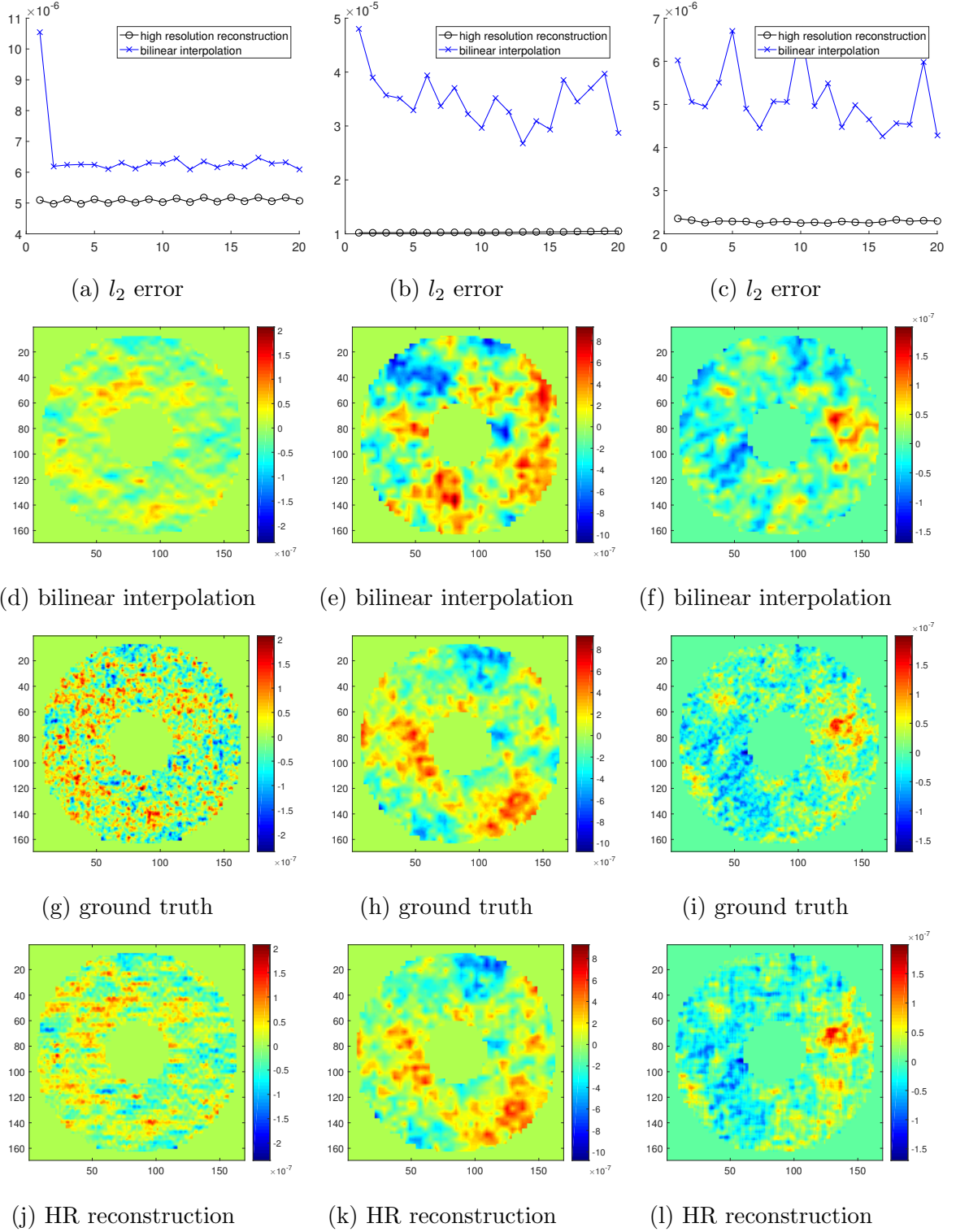


Figure 4: First column: simulation 1, second column: simulation 2, third column: simulation 3. The plots in the first row are  $l_2$ -errors of the reconstruction, with  $x$ -axis being the frame number. All the images from the second row to the last row are corresponding to  $t = 16$  (i.e., at the 16<sup>th</sup> time step) and show wavefronts in  $m$ .

In Figure 4d-4l, the images of the reconstruction by bilinear interpolation on the DM data, the true phase in high resolution and the high resolution reconstruction by the proposed method are given. As expected, the bilinear interpolations do not include the

fine details of the residual phase well. Our approach is able to recover some missing high frequency components in the data, therefore shows an improvement from the bilinear interpolation.

However, the high resolution reconstruction is limited by several factors. First, the time interval in which the TFF hypothesis holds is typically small. This limits the number of low resolution data and therefore set an upper bound for the resolution of the reconstruction. Second, the low resolution data is not acquired in a random manner. Instead, the motion vector is constant and the coarse grid points propagate in a fixed direction with a constant rate, which means that the 2D phase is not evenly sampled in a short time.

To have a closer look, Figure 5 displays the images of reconstruction errors for simulation 1 and simulation 3. The error images of the high resolution reconstruction have some special patterns. In Figure 5b, the pixels with bigger error are concentrated on some lines parallel to the vertical line, while in Figure 5d the relatively big errors are mainly distributed on the lines having an angle of 30 degrees with the vertical line. The directions of the lines coincide with the directions of the winds in both cases, which indicates that the phase at some grid points is not detected as well as other points over the process.

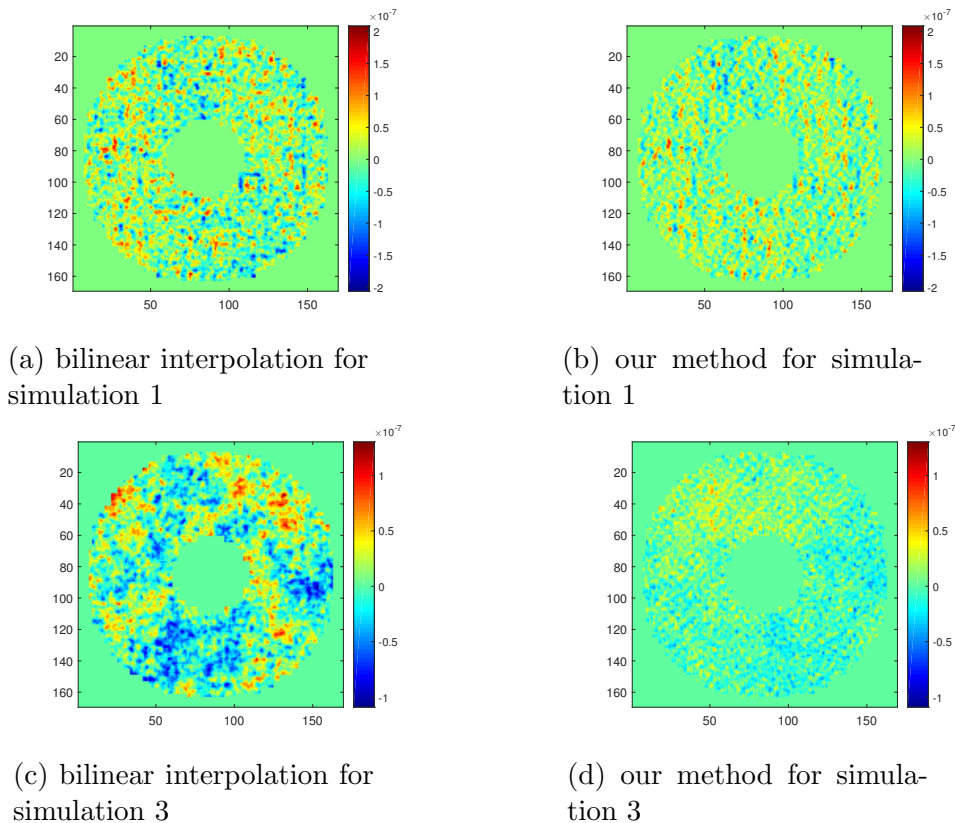


Figure 5: Reconstruction error images at  $t = 16$  of the bilinear interpolation and our method.

We take two additional steps to get closer to a realistic on sky scenario. For a two layer atmosphere and high photon flux, i.e., simulation 4, the performance of our algorithm is a bit worse than in the one layer case, as now the problem becomes a tomography problem.

As the wind directions for the two layers are different, recovering the information on each layer is much more challenging. Still, the improvement by of our algorithm ranges from 20% to 30%. The results for this case are plotted in Figure 6a.

The final step is to use the ESO-standard profile from Table 3 in simulation 5. In this case, the AO control algorithm still performs on a high level. Applying our algorithm leads to an improvement between 10% and 25%, showing that our model can cope with the multi-layered nature of the atmosphere. The results are shown in Figure 6b.

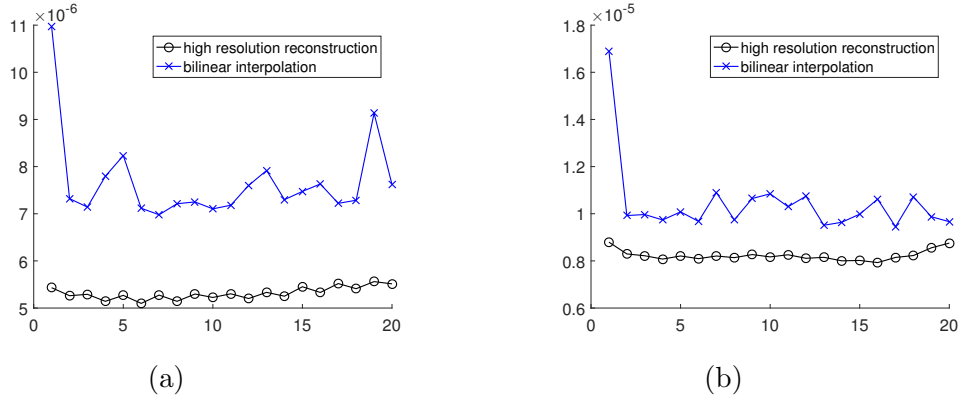


Figure 6: (a) and (b) are the  $l_2$ -errors of two methods for simulation 4 and simulation 5, respectively. The  $x$ -axis is the frame number.

### 5.3.2 Reconstructions with inexact wind velocities

We further study the performance of the proposed algorithms when the initial wind velocities (IWV) are imprecise. The adaptive wind velocity (AWV) algorithm is used. To make the results comparable to the previous reconstruction, we let the simulation settings be the same as before except that the precise wind velocities (PWV) are replaced by the imprecise ones. The proposed method is employed to on the five simulations and the IWV are assumed to have 10% to 20% error for all simulated cases.

For the first three simulations, Algorithm I is used and one wind velocity is computed for each simulation. The  $l_2$ -errors of the high resolution reconstructions are shown in Figures 7a - 7c. For comparison the previous test results on exact wind velocity cases are also displayed. According to the figures, with IWV the minimizer of (8) is computed and the corresponding  $l_2$ -error is significantly bigger than the ones obtained with the exact wind velocity at the first and last few frames, except for the low flux case (i.e., the second simulation). An IWV does not play a key role in the reconstruction accuracy in the low flux case where the observed data is very unreliable.

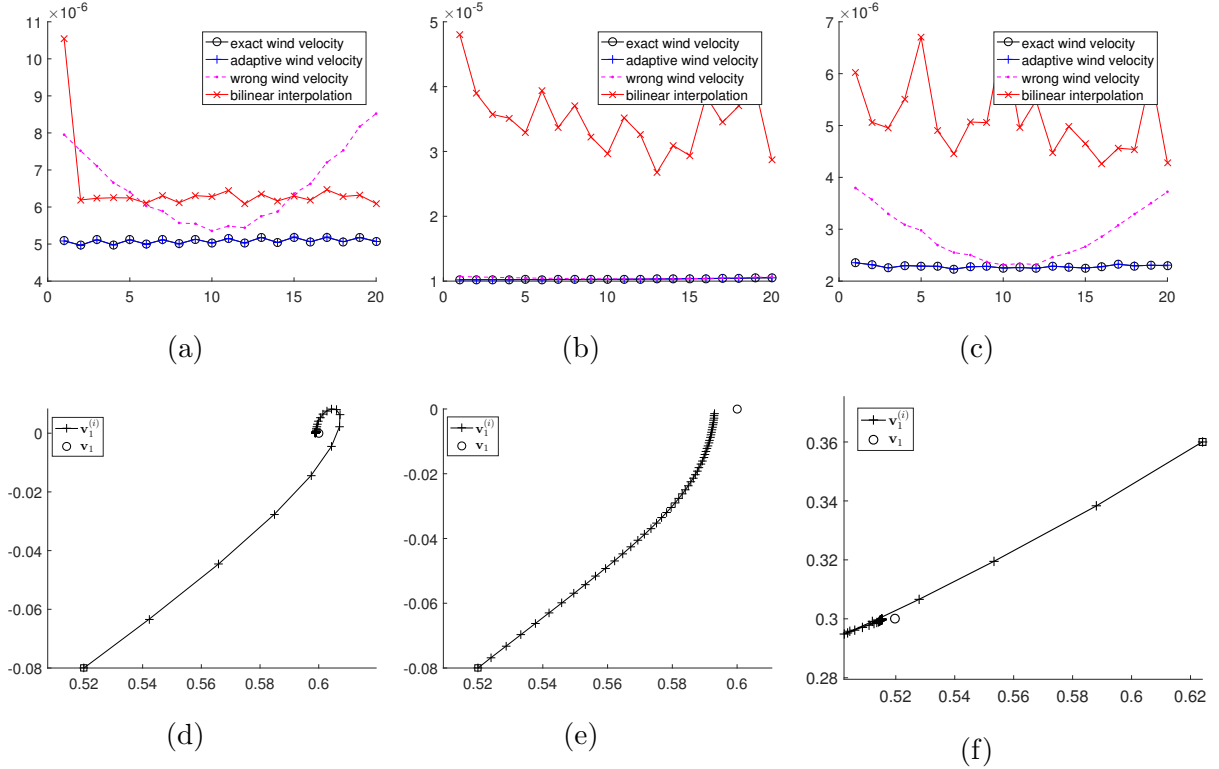


Figure 7: (a)-(c): The  $l_2$ -errors of the reconstructions for simulation 1 to 3 respectively. In these plots the  $x$ -axis is the frame number and  $y$ -axis is the  $l_2$ -error. The exact wind speed means reconstruction with fixed PWV, while the wrong wind speed means using IWV without adaption. (d)-(e): the adaptive wind velocity for simulation 1 to 3. The unit of the  $x$ - and  $y$ -axis is pixels per time step, given as  $25 \text{ m/s}$  (i.e., the number of high-resolution pixels (with length  $0.05 \text{ m}$ ) per time step (being  $1/500 \text{ s}$ )).

The estimated wind velocities at all iterations are plotted in Figure 7d-7f. The unit of the  $x$ - and  $y$ -axis is relating the number of high-resolution pixels (with length  $0.05 \text{ m}$ ) to the length of a time step, being  $1/500 \text{ s}$ , thus giving  $25 \text{ m/s}$ . In the high flux cases, Algorithm I starts with an initial wind velocity that has around 20% error, but finally outputs improved ones with less than 1% error. This implies that the algorithm is capable of extracting the wind velocity information from the AO data itself, and explains why it is still able to have a comparable reconstruction accuracy to the one obtained with the exact wind velocity, as shown Figure 7a and Figure 7c. In the low flux case, the error of the estimated wind velocity is reduced from 13.4% to around 1.4% as shown in Figure 7e.

For simulation 1 and simulation 3, the error images of the reconstruction from the last subsection, the reconstruction by the proposed algorithm and the reconstruction with fixed IWV are given Figure 8. Significantly larger errors can be observed from the algorithm without adaptive wind velocities while the proposed algorithm with adaptive velocities results in errors that look similar to the reconstructions with PWV.

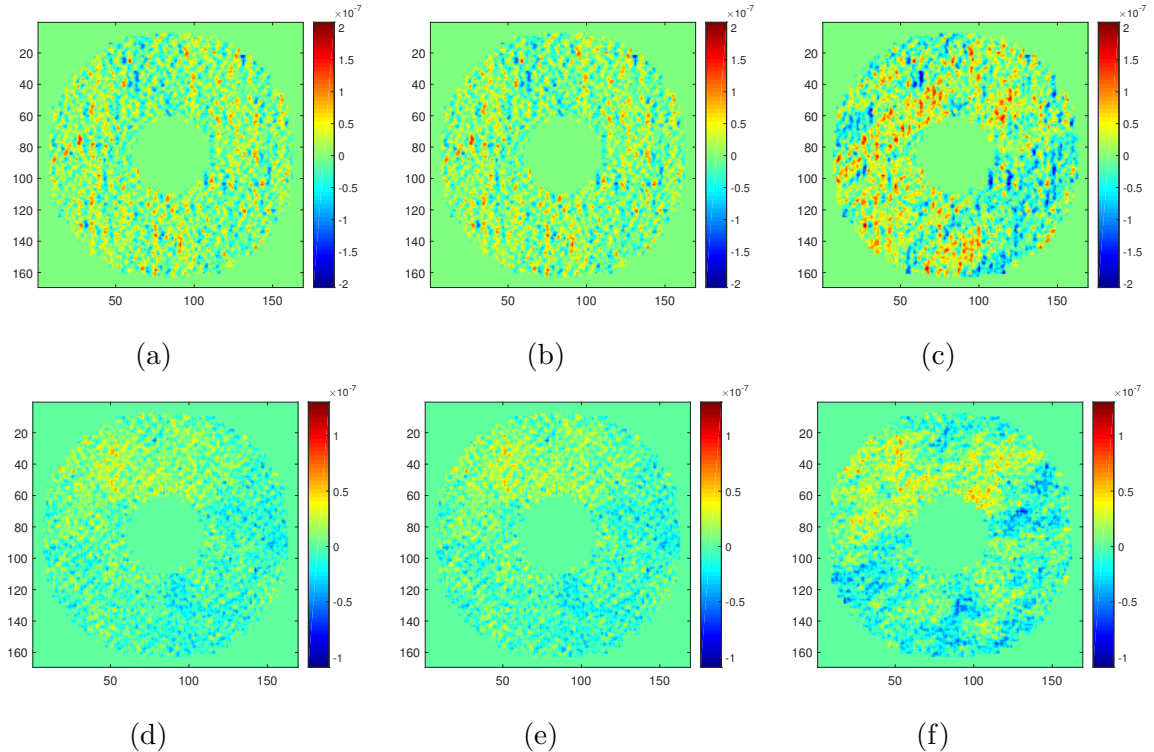


Figure 8: Error images of different reconstructions at  $t = 16$ . (a)-(c): with exact wind velocity, with adaptive wind velocity and without adaptive wind velocity for Simulation 1. (d)-(f): with exact wind velocity, adaptive wind velocity and without adaptive wind velocity for Simulation 3.

For the two layer case, i.e., simulation 4, we used Algorithm II which solves for the high resolution residual phase as well as the wind velocity for each of the two layers. IWVs  $\{\mathbf{v}_l^{(0)}\}$ , having around 10% to 20% error, are given. A reconstruction from (8) using the wrong wind velocities  $\{\mathbf{v}_l^{(0)}\}$  is also computed and a large error is observed at the first and last few frames as shown in Figure 9a. The reconstruction at the middle frames, however, has a close accuracy to reconstruction for the exact wind velocity case. On the other hand, Algorithm II with only inexact wind velocities  $\{\mathbf{v}_l^{(0)}\}$  gives almost the same accuracy as the solution of (8) with exact wind velocities. In Figure 9c, the wind velocity estimates for each of the two layers are displayed. It suggests that our algorithm can recover information of the wind velocities from the DM data itself using imprecise initial wind velocities.

Finally, Algorithm II is used to estimate estimates of the nine wind velocities for nine layers in the fifth simulation. Though in this case the  $l_2$ -error of the minimizer of (8) with the fixed IWV is still reasonably small compared to the minimizer with the PWV, Algorithm II can still make an improvement with the implementation of AWV. The resulting accuracy is shown in Figure 9b and the estimated wind velocities for all layers are given in Figure 9d. The algorithm fails to distinguish the layers with close wind velocities, such as the second layer and the sixth layer. The isolated wind velocities, however, are captured well, such as that of the fourth layer and the eighth layer. The reconstruction does not depend heavily on separating the wind velocities of those layers with similar motions, as the reconstruction accuracy shown in Figure 9b is still comparable to the one obtained with the PWV.

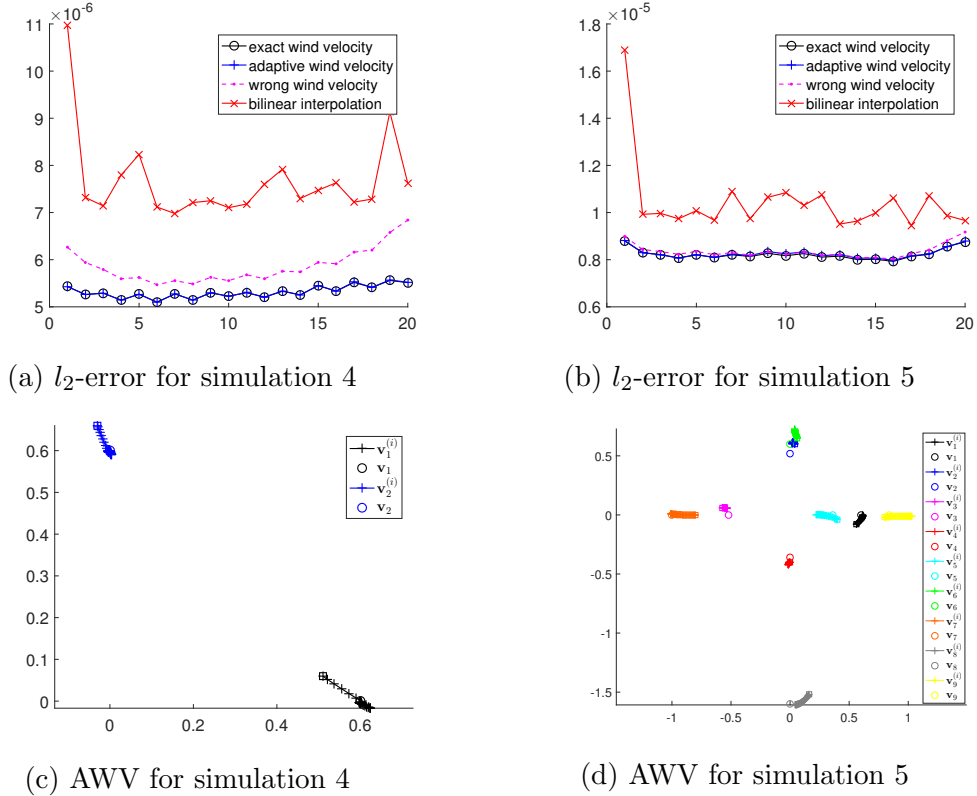


Figure 9: The  $l_2$ -errors and the estimated wind velocities for simulation 4 and 5.

## 6 Conclusion

We introduced a new method to derive a high resolution phase from coarse measurements in a closed loop AO system. Our approach is based on the Taylor Frozen Flow hypothesis and uses subsequently applied DM shapes in a minimization procedure to obtain a high resolution phase. For known wind velocities in the different atmospheric layers the functional to be minimized describes a tomography problem and can be solved with standard tools.

As the wind velocities might not be known in practice, we also investigated the case of imprecisely known wind velocities. This results in an augmented Lagrangian functional, which can be solved using an alternating direction method. Finally, we demonstrated the power of our method in numerical experiments under different atmospheric conditions. The  $l_2$ -error is clearly reduced by our method compared to a simple bilinear interpolation from a coarse to a fine grid in all cases. For the more realistic setting with nine atmospheric layers and imprecise knowledge of the wind velocities, the adaptive method outperforms the method using constantly wrong wind velocities and is close to exact knowledge of the wind velocities.

In practice, this method might be useful on the one hand for temporal control, using the calculated high resolution phase to predict the incoming phase (see [23] and the references therein for details on temporal control), and on the other hand a highly resolved phase could be useful for post processing, e.g., in PSF reconstruction methods as [31]. Bringing our method to this level requires investigating the behavior when scaled to the size of upcoming 40 m class telescopes like ESO's ELT. Furthermore, we will test our algorithm in end-to-end simulation tools for such telescopes to demonstrate the feasibility

for the AO community in more detail.

## Funding

The work of Roland Wagner and Ronny Ramlau was funded by the FWF Austrian Science Fund in the project “F 6805-N36: SFB Tomography Across the Scales” and by the Austrian Ministry of Research (Hochschulraumstrukturmittel) in the project “Beobachtungsorientierte Astrophysik in der E-ELT Ära”. The work of Rihuan Ke was funded by HKRGC Grant No. CUHK14306316 and by the FWF Austrian Science Fund in the Doctoral Program “Computational Mathematics” (W1214) – Project 8. The work of Raymond H. Chan was funded by HKRGC Grants No. CityU12500915, CityU14306316, HKRGC CRF Grant C1007-15G, and HKRGC AoE Grant AoE/M-05/12.

## References

- [1] N. Bharmal, U. Bitenc, A. Basden, R. Myers, and N. Dipper. “A hierarchical wavefront reconstruction algorithm for gradient sensors”. In: *Third AO4ELT Conference – Adaptive Optics for Extremely Large Telescopes*. 2013. DOI: 10.12839/AO4ELT3.13280.
- [2] U. Bitenc, A. Basden, N. Ali Bharmal, T. Morris, N. Dipper, E. Gendron, F. Vidal, D. Gratadour, G. Rousset, and R. Myers. “On-sky tests of the CuReD and HWR fast wavefront reconstruction algorithms with CANARY”. In: *Monthly Notices of the Royal Astronomical Society* 448.2 (2015), pp. 1199–1205.
- [3] B. Boyd, N. Parikh, E. Chu, B. Peleato, J. Eckstein, et al. “Distributed optimization and statistical learning via the alternating direction method of multipliers”. In: *Foundations and Trends® in Machine Learning* 3.1 (2011), pp. 1–122.
- [4] R.H. Chan, Z. Shen, and T. Xia. “A framelet algorithm for enhancing video stills”. In: *Applied and Computational Harmonic Analysis* 23.2 (2007), pp. 153–170.
- [5] R.H. Chan, X. Yuan, and W. Zhang. “Point-spread function reconstruction in ground-based astronomy by  $l^1 - l^p$  model”. In: *JOSA A* 29.11 (2012), pp. 2263–2271.
- [6] Q. Chu, S. Jefferies, and J.G. Nagy. “Iterative wavefront reconstruction for astronomical imaging”. In: *SIAM Journal on Scientific Computing* 35.5 (2013), S84–S103.
- [7] R. Davies and M. Kasper. “Adaptive optics for astronomy”. In: *Annual Review of Astronomy and Astrophysics* 50 (2012), pp. 305–351.
- [8] L. Dykes, R. Ramlau, L. Reichel, K.M. Soodhalter, and R. Wagner. “Lanczos-based fast blind deconvolution methods”. In: *RICAM Report 2017-27* (2017).
- [9] B.L. Ellerbroek. “Efficient computation of minimum-variance wave-front reconstructors with sparse matrix techniques”. In: *Journal of the Optical Society of America A* 19.9 (2002), pp. 1803–1816.
- [10] B.L. Ellerbroek and C.R. Vogel. “Inverse problems in astronomical adaptive optics”. In: *Inverse Problems* 25.6 (2009), p. 063001.

- [11] S. Farsiu, M. Elad, and P. Milanfar. “Multiframe demosaicing and super-resolution of color images”. In: *IEEE transactions on image processing* 15.1 (2006), pp. 141–159.
- [12] D.L. Fried. “Least-square fitting a wave-front distortion estimate to an array of phase-difference measurements”. In: *Journal of the Optical Society of America* 67.3 (1977), pp. 370–375.
- [13] C. Gilliam and T. Blu. “Local all-pass filters for optical flow estimation”. In: *Acoustics, Speech and Signal Processing (ICASSP), 2015 IEEE International Conference on*. IEEE. 2015, pp. 1533–1537.
- [14] C. Gilliam and T. Blu. “Local all-pass geometric deformations”. In: *IEEE Transactions on Image Processing* 27.2 (2018), pp. 1010–1025.
- [15] J.W. Goodman. *Introduction to Fourier optics*. Roberts and Company Publishers, 2005.
- [16] T. Helin and M. Yudytskiy. “Wavelet methods in multi-conjugate adaptive optics”. In: *Inverse Problems* 29.8 (2013), p. 085003. URL: <http://stacks.iop.org/0266-5611/29/i=8/a=085003>.
- [17] A.K. Jain. *Fundamentals of digital image processing*. Prentice-Hall, Inc., 1989.
- [18] S.M. Jefferies and M. Hart. “Deconvolution from wave front sensing using the frozen flow hypothesis”. In: *Optics express* 19.3 (2011), pp. 1975–1984.
- [19] A. Kolmogorov. “The local structure of turbulence in incompressible viscous fluid for very large Reynolds numbers”. In: *Dokl. Akad. Nauk SSSR*. Vol. 30. 4. 1941, pp. 299–303.
- [20] M. Le Louarn, C. Véraud, V. Korhonen, N. Hubin, and E. Marchetti. “Adaptive optics simulations for the European Extremely Large Telescope”. In: *Proc. SPIE 6272, Advances in Adaptive Optics II*. 2006.
- [21] K. Nasrollahi and T.B. Moeslund. “Super-resolution: a comprehensive survey”. In: *Machine vision and applications* 25.6 (2014), pp. 1423–1468.
- [22] A. Neubauer. “A new cumulative wavefront reconstructor for the Shack-Hartmann sensor”. In: *J. Inv. Ill-Posed Problems* 21 (2013), pp. 451–476.
- [23] M. Pöttinger, R. Ramlau, and G. Auzinger. “A new Temporal Control Approach for SCAO Systems”. In: *Inverse Problems* submitted (2019).
- [24] M.C. Roggemann, B.M. Welsh, and B.R. Hunt. *Imaging through turbulence*. CRC press, 1996.
- [25] M. Rosenstainer. “Cumulative Reconstructor: fast wavefront reconstruction algorithm for Extremely Large Telescopes”. In: *Journal of the Optical Society of America A* 28.10 (2011), pp. 2132–2138.
- [26] M. Rosenstainer. “Wavefront reconstruction for extremely large telescopes via CuRe with domain decomposition”. In: *Journal of the Optical Society of America A* 29.11 (2012), pp. 2328–2336.
- [27] G. Taylor. “The spectrum of turbulence”. In: *Proceedings of the Royal Society of London. Series A, Mathematical and Physical Sciences* 164.919 (1938), pp. 476–490.

- [28] E. Thiébaud and M. Tallon. “Fast minimum variance wavefront reconstruction for extremely large telescopes”. In: *Journal of the Optical Society of America A* 27.5 (2010), pp. 1046–1059.
- [29] J.-P. Véran, F. Rigaut, H. Maître, and D. Rouan. “Estimation of the adaptive optics long exposure point spread function using control loop data”. In: *Journal of the Optical Society of America A* 14.11 (1997), pp. 3057–3069. DOI: 10.1364/JOSAA.14.003057.
- [30] R. Wagner. “From Adaptive Optics systems to Point Spread Function Reconstruction and Blind Deconvolution for Extremely Large Telescopes”. PhD thesis. Johannes Kepler University Linz, 2017.
- [31] R. Wagner, C. Hofer, and R. Ramlau. “Point spread function reconstruction for Single-conjugate Adaptive Optics”. In: *Journal of Astronomical Telescopes, Instruments, and Systems* 4.4 (2018), p. 049003. DOI: 10.1117/1.JATIS.4.4.049003.
- [32] R. Wagner, A. Neubauer, and R. Ramlau. “Simulation results for a finite element-based cumulative reconstructor”. In: *Journal of Astronomical Telescopes, Instruments, and Systems* 3.4 (2017), p. 049001. DOI: 10.1117/1.JATIS.3.4.049001.
- [33] H. Weichel. *Laser beam propagation in the atmosphere*. Vol. 3. SPIE press, 1990.
- [34] M. Yudytskiy, T. Helin, and R. Ramlau. “Finite element-wavelet hybrid algorithm for atmospheric tomography”. In: *Journal of the Optical Society of America A* 31.3 (2014), pp. 550–560.
- [35] M. Zhariy, A. Neubauer, M. Rosensteiner, and R. Ramlau. “Cumulative Wavefront Reconstructor for the Shack-Hartman Sensor”. In: *Inverse Problems and Imaging* 5.4 (2011), pp. 893–913.